INTERNATIONAL JOURNAL FOR NUMERICAL METHODS IN FLUIDS, VOL. 24, 291–317 (1997)

A FINITE ELEMENT MODEL FOR THE SIMULATION OF DENSE GAS DISPERSION IN THE ATMOSPHERE

A. I. SAYMA

Centre of Vibration Engineering, Department of Mechanical Engineering, Imperial College, London SW7 2BX, U.K.

AND

P. L. BETTS

Department of Mechanical Engineering, UMIST, PO Box 88, Manchester M60 1QD, U.K.

SUMMARY

A state-of-the-art model is developed for the simulation of the dispersion of hazardous toxic or flammable gases heavier than air in the atmosphere. The model depends on solving the Reynolds-averaged Navier–Stokes equations in addition to the energy equation and a species concentration equation for the contaminant gas. Turbulence closure is achieved by using a buoyancy-extended version of the standard k–ϵ two-equation model. The buoyancy extension is introduced to account for the anisotropic turbulent viscosity resulting from the strong stratification introduced by the dense gas clouds. The spatial discretization is achieved via the Galerkin finite element method, while the solution is advanced in time using the forward Euler method. A special element layer is introduced in the near-ground region to bridge the gap between the solid wall and the main solution domain where the turbulence model can be applied. This special element layer eliminates the need to apply the wall function in the standard way where any oscillations in the pressure field could contaminate the velocity solution. The model was tested against the Burro-8 field trial and could predict the experiment satisfactorily to within the experimental uncertainties of the reported results.

KEY WORDS: Navier–Stokes equations; dense gas dispersion; density stratification; anisotropic turbulent viscosity

1. INTRODUCTION

Many toxic or flammable gases are stored and transported at high pressure or low temperature or both. If during the course of manufacture, transport or storage of these gases an accidental release to the atmosphere occurs, the consequences could be fatal. By virtue of their molecular weight or temperature at release to the atmosphere, some gases could be denser than air. This results in a dense gas cloud which rolls near the ground for some time before dispersing, which increases the risks of suffocation, fires or explosions. In the past 30 years, several accidents of this category have been recorded (see e.g. Reference 1) and have attracted attention to a problem which was not addressed before. The dispersion of dense gas clouds is complicated in nature compared with passive pollutants or buoyant plumes. It will depend on the topography of the region, which might include buildings,

CCC 0271–2091/97/030291–27

Received November 1995
Revised April 1996

industrial installations, hills, valleys, escarpments and mountains. Because of its heavy weight, the gas slumps to the ground, forming a flat shape with horizontal dimensions much larger than the height. The strong density stratification resulting from large temperature gradients reduces turbulence levels significantly and inhibits turbulence mixing, causing a long delay in the dispersion of the cloud.

The problem of estimating the consequences of dense gas releases in the atmosphere is of prime importance in the assessment of the safety of industrial installations and transport systems. The task of performing such an assessment has been introduced as a regulatory requirement in many countries. The assessment procedures depend mainly on experience from previous accidents, experimental tests conducted in laboratory or field tests and mathematical models. The present paper considers the mathematical modelling of the problem.

There are a large number of models in the literature which range from simple box models to sophisticated differential models. For a full survey of these models the reader is referred to References 2 and 3. In summary, mathematical models can be classified into two broad categories: integral plume models and differential models. Integral plume models mainly prescribe the general shape of the cloud and use empirical or semiempirical relations to calculate the concentration of the dense gas. Differential models resort to solving the primary equations that control the flow field and the dense gas transport and thus have a much lower degree of empiricism. The present model falls within the second class. These models were developed to overcome the limitations of integral plume models by reducing the amount of empirical input. However, differential models require much larger computational effort and their practical application will require the most efficient and robust numerical procedures in addition to retaining generality and accuracy, which would be required in many situations such as predicting cases which cannot be modelled using simple models, providing further understanding of the aspects of dense gas dispersion and the tuning and calibration of simple models.

In the present study the dense gas dispersion model FEMSET, developed earlier by Betts and Haroutunian,[4] has been further developed and tested. This differential-type model is based on the solution of the equations of momentum, continuity and energy and a species concentration equation to predict the dispersion of the contaminant gas. A buoyancy-extended anisotropic k–ϵ turbulence model is used for the closure of the averaged system of flow equations. The numerical procedure employs the finite element method for spatial discretization, which is convenient for modelling complex flow domains. The forward Euler method is used for advancing the solution in time for computational economy. A special near-wall layer of elements is used to apply the wall functions indirectly, since in the earlier model the direct application of the wall laws led to instabilities resulting from the interaction of the oscillatory pressure field near the wall and the velocity field. The special element layer proved to combine accuracy and solution economy in the modelling of the near-wall region.

The model has been tested against a wide range of 2D flows[5,6] and has proved to be a robust two-equation flow solver. Dense gas dispersion tests were conducted to simulate field and laboratory tests[4,7] and in the present study the extended model was used to simulate the Burro- 8[8] field dense gas dispersion and could predict the trial qualitatively and quantitatively to a satisfactory accuracy.

2. NUMERICAL MODEL

The instantaneous flow equations for a two-component mixture, which represent the conservation of mass, momentum, energy and species concentration expressed in Eulerian form with terms of order of magnitude relevant to dense gas dispersion problems, have been presented by many authors (see e.g. References 9 and 10). These equations expressed in tensor notation can be written as

$$\frac{\partial \rho}{\partial t}+\frac{\partial}{\partial x_j}(\rho u_j)=0, \tag{1a}$$

$$\frac{\partial}{\partial t}(\rho u_i)+\frac{\partial}{\partial x_j}(\rho u_i u_j)=-\frac{\partial p}{\partial x_i}+(\rho-\rho_{\mathrm{o}})g_i, \tag{1b}$$

$$\frac{\partial}{\partial t}(\rho h)+\frac{\partial}{\partial x_j}(\rho u_j h)=S_h, \tag{1c}$$

$$\frac{\partial}{\partial t}(\rho c)+\frac{\partial}{\partial x_j}(\rho u_j c)=0, \tag{1d}$$

where x_i, $i=1, 2, 3$, refer to co-ordinates x, y and z respectively in the Cartesian co-ordinate system. The corresponding velocity components u_i, $i=1, 2, 3$, which are usually termed u, v and w respectively, refer to the velocity components in the above directions. The air–gas mixture density is termed ρ and is given by the equation of state (equation (2)). Moreover, p is the pressure deviation from a reference pressure at a reference density ρ_{o} and S_h is the heat source/sink term in the energy equation due to external effects such as radiation absorption.

The above system of equations requires the calculation of the mixture density and enthalpy, which are given by the constitutive relations

$$\rho=\frac{(P_{\mathrm{o}}-\rho_{\mathrm{o}}gz)}{RT[c/M_{\mathrm{g}}+(1-c)/M_{\mathrm{a}}]}, \tag{2}$$

$$h=c_{\mathrm{p}}T, \tag{3}$$

where

$$c_{\mathrm{p}}=cc_{\mathrm{pg}}+(1-c)c_{\mathrm{pa}}. \tag{4}$$

In deriving this system of equations, it was assumed that the air–gas mixture is essentially dry and in the gaseous phase, no chemical reactions take place and pressure work and viscous dissipation terms are negligible in the energy equation. Additionally, Coriolis acceleration terms due to ground rotation and diffusion terms were neglected in the momentum equations. The last assumptions can be justified by performing an order-of-magnitude analysis on the basic flow equations.[2]

The density is calculated in equation (2) using $P_{\mathrm{o}}-\rho_{\mathrm{o}}gz$ instead of the thermodynamic pressure $P=p+P_{\mathrm{o}}-\rho_{\mathrm{o}}gz$. The value of P_{o} is typically 1 atm ($\approx 101{,}325$ N m^{-2}) and p is $O(10^2)$–$O(10^3)$ N m^{-2} in typical dense gas flows. Thus density changes due to pressure changes are 0·1%–1% compared with those due to temperature and concentration changes of up to 50%. Therefore P in the equation of state can be replaced by $P_{\mathrm{o}}-\rho_{\mathrm{o}}gz$ with little loss of accuracy. This decoupling of density from the pressure deviation p renders the flow incompressible (in the classical concept of $\partial p/\partial\rho\rightarrow\infty$) and suppresses the pressure waves which might otherwise appear as a solution of the above system of equations. These pressure waves would have very small time scales, associated with sonic phase velocities, that would require very small time steps if not suppressed, which would consequently increase the computational cost considerably. It is worth noting that using the Boussinesq approximation to suppress pressure waves, whereby density variations are neglected except in the buoyancy term in the momentum equation,[11] is inadequate in dense gas dispersion problems owing to the large density variations involved.[3] An alternative way of suppressing pressure waves is the anelastic approximation ($\partial\rho/\partial t=0$) which is used in the dense gas dispersion model FEM3.[12]

Solving the above system of equations numerically in its instantaneous form is a formidable task owing to the fine grids required to resolve the smallest scales of turbulence. To overcome this problem, statistical averaging is introduced. After performing statistical averaging on the equations and neglecting terms containing a fluctuating density component, they can be written as

$$\frac{\partial\rho}{\partial t}+\frac{\partial(\rho u_j)}{\partial x_j}=0, \tag{5a}$$

$$\frac{\partial(\rho u_i)}{\partial t}+\frac{\partial(\rho u_i u_j)}{\partial x_j}=-\frac{\partial p}{\partial x_i}-(\rho-\rho_{\mathrm{o}})g_i-\frac{\partial(\rho\overline{u_i'u_j'})}{\partial x_j}, \tag{5b}$$

$$\frac{\partial(\rho h)}{\partial t}+\frac{\partial(\rho u_j h)}{\partial x_j}=S_h-\frac{\partial(\rho\overline{u_j'h'})}{\partial x_j}, \tag{5c}$$

$$\frac{\partial(\rho c)}{\partial t}+\frac{\partial(\rho u_j c)}{\partial x_j}=-\frac{\partial(\rho\overline{u_j'c'})}{\partial x_j}. \tag{5d}$$

Note that the same notation has been used for the average quantities as for the instantaneous quantities for simplicity of notation. Any symbol will refer consequently to the averaged value unless stated otherwise. Moreover, the primed variables refer to the fluctuating components of the corresponding variables.

It is important to note here that it has been assumed that the turbulent density fluctuations produce negligibly small dynamical effects in the mean transport equations. Thus, in deriving equation (5), statistical correlations involving the fluctuating density component ρ' have been omitted. These omissions can be partially justified by reference to the Boussinesq approximation for density variations. Here the Boussinesq approximation can be thought of as having been applied to the fluctuating density component only, while the dynamic effects resulting from mean density variations in both space and time are fully allowed for.

As a result of the averaging process the following unknown quantities appear in the mean flow equations: $\rho\overline{u_i'u_j'}$, $\rho\overline{u_j'h'}$ and $\rho\overline{u_j'c'}$. The first term represents the turbulent fluxes of momentum and is usually termed the Reynolds stress tensor. The second term represents the turbulent flux of energy and the third term represents the turbulent flux of species concentration. The averaging process thus introduces 12 unknown variables in the mean flow equations. These values are usually approximated by the use of turbulence models, which is the subject of the following subsection.

2.1. Turbulence model

The turbulence model used to provide additional equations to describe the temporal and spatial evolution of turbulent fluxes is an extension of the standard k–ϵ model. The standard k–ϵ model uses the eddy viscosity concept to represent the turbulent fluxes by assuming that these turbulent fluxes are proportional to the mean gradients of the related variables. In the present extension the generalized eddy viscosity concept is used, where the scalar or isotropic diffusivities provided by the standard k–ϵ model are replaced by tensor diffusivities as follows:

$$-\rho\overline{u_i'u_j'}=\rho K_{ijlm}\left(\frac{\partial u_l}{\partial x_m}+\frac{\partial u_m}{\partial x_l}\right)-\tfrac{2}{3}\rho k\delta_{ij}, \tag{6a}$$

$$-\rho\overline{u_i'h'}=\rho K_{ij}^{h}\frac{\partial h}{\partial x_j}, \tag{6b}$$

$$-\rho\overline{u_i'c'}=\rho K_{ij}^{c}\frac{\partial c}{\partial x_j}, \tag{6c}$$

where K_{ijlm} is fourth-order eddy viscosity tensor and K_{ij}^{h} and K_{ij}^{c} are second-order tensors denoting the turbulent diffusivities for energy and species concentration respectively. These tensors are determined partly from the application of physical constraints and partly from the imposition of arbitrary constraints. These constraints are detailed in Reference 2. The tensor K_{ijlm} takes the form

$$K_{ijlm} \rightarrow c_{\mu}\frac{k^2}{\epsilon}\left\{\begin{matrix} 1 & \overline{v'^2}/\overline{w'^2} & 1 \\ \overline{v'^2}/\overline{w'^2} & 1 & 1 \\ 1 & 1 & 1 \end{matrix}\right\}. \tag{7}$$

The fluctuating velocity ratio $\overline{v'^2}/\overline{w'^2}$ has been derived from the algebraic stress model of Gibson and Launder,[13] where in this context only v' is normal to the *local* mean horizontal component of velocity. This ratio is given by

$$\frac{\overline{v'^2}}{\overline{w'^2}} = (5{\cdot}4+3f)\frac{0{\cdot}518+0{\cdot}66f+0{\cdot}277f\,\overline{w'^2}/k+(0{\cdot}037+0{\cdot}0666f)[-b/(s+b)]}{2\{1{\cdot}4-0{\cdot}36f-(1{\cdot}4+0{\cdot}36f)[-b/(s+b)]\}}, \tag{8}$$

$$\frac{\overline{w'^2}}{k} = \frac{2}{5{\cdot}4+3f}\left[1{\cdot}4+0{\cdot}36f-(1{\cdot}4+0{\cdot}3f)\left(\frac{-b}{s+b}\right)\right], \tag{9}$$

$$f = \frac{c_{\mu}^{3/4}k^{3/2}}{\kappa z\epsilon}, \tag{10}$$

where f is the wall-damping function which in this form is due to Rodi.[15] The source term s and the buoyancy term b are detailed below. In equation (7), k and ϵ are evaluated from the differential equations

$$\rho\frac{\partial k}{\partial t}+U_j\frac{\partial k}{\partial x_j}=\frac{\partial}{\partial x_i}\left(\rho K_{ij}^{k}\frac{\partial k}{\partial x_j}\right)+s+b-\rho\epsilon, \tag{11a}$$

$$\rho\frac{\partial \epsilon}{\partial t}+U_j\frac{\partial \epsilon}{\partial x_j}=\frac{\partial}{\partial x_i}\left(\rho K_{ij}^{\epsilon}\frac{\partial \epsilon}{\partial x_j}\right)+c_{\epsilon 1}\frac{\epsilon}{k}[s+(1-c_{\epsilon 3})b]-c_{\epsilon 2}\rho\frac{\epsilon^2}{k}, \tag{11b}$$

where U_i is defined as ρu_i. Furthermore, the source term and the buoyancy term are written as

$$s=\rho K_{ijlm}\left(\frac{\partial u_l}{\partial x_m}+\frac{\partial u_m}{\partial x_l}\right)\frac{\partial u_i}{\partial x_j}, \tag{12}$$

$$b=-K_{ij}^{\rho}\frac{\partial \rho}{\partial x_j}g_i. \tag{13}$$

The eddy diffusivity tensors in equations (6b), (6c), (11) and (13) are given by

$$Pr_hK_{ij}^{h}=Sc_cK_{ij}^{c}=Pr_{\rho}K_{ij}^{\rho}=Pr_kK_{ij}^{k}=Pr_{\epsilon}K_{ij}^{\epsilon}=c_{\mu}\frac{k^2}{\epsilon}\begin{bmatrix}\overline{v'^2}/\overline{w'^2} & 0 & 0\\ 0 & \overline{v'^2}/\overline{w'^2} & 0\\ 0 & 0 & 1\end{bmatrix}, \tag{14}$$

where

$$Pr_h=Sc_c=Pr_{\rho}=Pr=\begin{cases}\dfrac{1{\cdot}015+8{\cdot}85\zeta}{1{\cdot}0+6{\cdot}45\zeta} & \text{for } \zeta=\dfrac{z}{L}\geq 0,\\[2ex] \dfrac{1{\cdot}015(1{\cdot}0-20{\cdot}6\zeta)^{1/4}}{(1{\cdot}0-12{\cdot}35\zeta)^{1/2}} & \text{for } \zeta=\dfrac{z}{L}<0\end{cases} \tag{15}$$

and the Monin–Oboukhov length scale becomes

$$L = \rho c_\mu^{3/2} k^3 \epsilon^{-3/2} \left[\left(\frac{\partial u}{\partial z} + \frac{\partial w}{\partial x} \right)^2 + \left(\frac{\partial v}{\partial z} + \frac{\partial w}{\partial y} \right)^2 \right]^{3/4} \Big/ \kappa b. \tag{16}$$

The above turbulence model constants are $c_\mu = 0{\cdot}09$, $Pr_k = 1{\cdot}0$, $Pr_\epsilon = 1{\cdot}25$, $c_{\epsilon 1} = 1{\cdot}45$, $c_{\epsilon 2} = 1{\cdot}9$ and $c_{\epsilon 3} = -0{\cdot}8$ for $\zeta < 0$ and $2{\cdot}15$ for $\zeta > 0$, where the constant $c_{\epsilon 3}$ in the model has been obtained by Betts and Haroutunian[5] from computer optimization using atmospheric surface layer data.

3. NUMERICAL METHODOLOGY

The numerical methodology implemented in the model depends on discretizing the system of equations governing the flow and turbulent quantities using the Galerkin finite element method. Upon discretizing the system of equations, it can be written in the symbolic form

$$\mathbf{M}\dot{\mathbf{U}} - \mathbf{C}\mathbf{p} = \mathbf{f}, \tag{17a}$$

$$\mathbf{D}\mathbf{U} = -\mathbf{M}_\rho \dot{\boldsymbol{\rho}}, \tag{17b}$$

$$\mathbf{M}_h \dot{\mathbf{h}} = \mathbf{f}_h, \tag{17c}$$

$$\mathbf{M}_c \dot{\mathbf{c}} = \mathbf{f}_c, \tag{17d}$$

$$\mathbf{M}_k \dot{\mathbf{k}} = \mathbf{f}_k, \tag{17e}$$

$$\mathbf{M}_\epsilon \dot{\mathbf{E}} = \mathbf{f}_\epsilon, \tag{17f}$$

where trilinear (bilinear in 2D) shape functions are used to represent all variables except for the piecewise constant shape function for pressure.

The time integration scheme was chosen to be fully explicit for reasons of simplicity and storage and computer time economy. The forward Euler method (FEM) has been adopted and applied in conjunction with the balancing tensor diffusivity (BTD) technique to march the system of ordinary differential equations in time. The BTD technique is applied to counter the negative diffusion arising from the first-order time truncation error associated with the FEM, by adding a positive diffusivity tensor of equal magnitude. For a full derivation and discussion of the BTD technique see Reference 16.

Application of the above method to the system of matrix equation (17) leads to the explicit decoupled equations

$$\mathbf{U}^{n+1} = \mathbf{U}^n + \Delta t \mathbf{M}^{-1}(\mathbf{f}^n + \mathbf{C}\mathbf{p}^n), \tag{18a}$$

$$\mathbf{h}^{n+1} = \mathbf{h}^n + \Delta t (\mathbf{M}_h^{-1})^n \mathbf{f}_h^n, \tag{18b}$$

$$\mathbf{c}^{n+1} = \mathbf{c}^n + \Delta t (\mathbf{M}_c^{-1})^n \mathbf{f}_c^n, \tag{18c}$$

$$\mathbf{k}^{n+1} = \mathbf{k}^n + \Delta t (\mathbf{M}_k^{-1})^n \mathbf{f}_k^n, \tag{18d}$$

$$\boldsymbol{\epsilon}^{n+1} = \boldsymbol{\epsilon}^n + \Delta t (\mathbf{M}_\epsilon^{-1})^n \mathbf{f}_\epsilon^n, \tag{18e}$$

where the load vectors have been modified by the addition of the BTD contributions. It should be noted that the matrices **M**, $\mathbf{M}_\rho$, **C** and **D** are functions only of the global basis functions and the global weighting functions and are therefore constant for a given mesh. All other matrices and load vectors are time-dependent and have to be assembled at every time step. It is also worth mentioning that all mass matrices have been lumped (i.e. row sum on diagonal) to make their inversion cost-effective. It has been shown by Gresho *et al.*[17] that mass matrix lumping leads to a degradation of the accuracy of the transient solution, although the steady state solution is not affected. However, in the formulation of FEMSET the drawback of mass lumping was considered to be outweighed by the enormous gains in reducing the computational effort. The consistent mass matrices are banded and sparse and their inversion requires a large amount of computer time. The sink terms in the k and ϵ equations have been treated in a pseudoimplicit manner to enhance numerical stability.[2]

By requiring the continuity equation (18a) to be satisfied at time $n+1$ and combining the resulting equation with the momentum equation, the following Poisson equation for pressure is obtained:

$$(\mathbf{C}^{\mathrm{T}}\mathbf{M}^{-1}\mathbf{C})\mathbf{p}^{n} = -\mathbf{C}^{\mathrm{T}}\mathbf{M}^{-1}\mathbf{f}^{n} + \frac{1}{\Delta t}[(\mathbf{C}^{\mathrm{T}} - \mathbf{D})\mathbf{U}^{n+1} - \mathbf{C}^{\mathrm{T}}\mathbf{U}^{n}] - \frac{1}{(\Delta t)^{2}}\mathbf{M}_{\rho}(\boldsymbol{\rho}^{n+1} - \boldsymbol{\rho}^{n}). \tag{19}$$

It should be noted that the right-hand side of equation (19) differs from that of Chan,[12] who made use of the anelastic approximation.

The resulting pressure matrix $\mathbf{C}^{\mathrm{T}}\mathbf{M}^{-1}\mathbf{C}$ is banded and symmetric and thus only half of it needs to be stored. It has been noted that this matrix depends only on the mesh geometry and thus can be assembled once, reduced and used throughout the solution.

The solution procedure follows from the above pressure matrix and can be summarized in the following steps.

1. The pressure matrix is assembled, reduced and stored.
2. The field variables are supplied as initial conditions at time $t=0$.
3. From the latest field variables the mass matrices associated with h, c, k and ϵ and all the load vectors are assembled.
4. The enthalpy, mass fraction, k and ϵ fields are advanced in time using their corresponding equations.
5. The density is calculated at the new time level from the equation of state (equation (2)) using the values of enthalpy and mass concentration from step 4.
6. The right-hand side of the pressure equation is evaluated.
7. The pressure is obtained by back substitution using the reduced pressure matrix and the calculated right-hand side.
8. The velocity field is advanced to the new time level.
9. The new time step is obtained from the stability criteria (stability criteria are discussed below) and steps 3–9 are repeated.

A necessary stability condition for the integration of an advection– diffusion equation using the FEM is that the equivalent exact equation, advanced by a Taylor series using the FEM, should be well posed. This requires the diffusivity tensor to be positive definite. The complete stability analysis of the advection–diffusion equation using forward Euler and Galerkin spatial discretization is difficult to perform. Here the practice adopted by Gresho *et al.*[16] for determining a suitable time step for the coupled, non-linear three-dimensional flow equations is employed in FEMSET. This consists of applying the stability relations

$$\Delta t \leqslant 1/(2K_i/\Delta x_i^2), \tag{20a}$$

$$\Delta t \leqslant [1/(u_i/\Delta x_i)^2]^{1/2}, \tag{20b}$$

$$\Delta t \leqslant \Delta x^2/K_i\{1 + [1 + (u_i\Delta x_i/K_i)^2]^{1/2}\} \quad \text{(no summation on } i) \tag{20c}$$

at every grid point for each of the transport equations and taking the smallest time step that results. In these equations, K_i and x_i are the diffusivity and average element size in the i-direction.

All the integrations were done by $2\times2\times2$ Gaussian quadrature in the pressure matrix assembly and in the load vector assembly.

3.1. The near-ground treatment

In the initial stages of model development the wall laws were applied through the wall functions at a distance δ from the wall to avoid the near-wall region where sharp gradients of variables exist, which requires a very fine mesh to be predicted reasonably. It also requires another turbulence model, since the standard k–ϵ model used in the domain cannot be applied in the near-wall region. Application of the wall function in this way led to interaction between the oscillatory pressure mode near the ground and the velocity field, over course meshes, through the wall function, in irregular topography problems and to failure of the simulations.

To overcome this problem and resolve the steeply varying quantities near the wall, a one-element-thick layer of special elements was used to span the region between the domain that contains all equations and the real boundary. The direction normal to the wall was aligned with one of the co-ordinate directions of the element, here termed n_{w}. The shape function in the n_{w}-direction is derived from the rough wall boundary layer velocity profile

$$u^{+}=\frac{u}{u_{*}}=\frac{1}{\kappa}\ln\left(\frac{z+z_{\mathrm{o}}}{z_{\mathrm{o}}}\right), \tag{21}$$

where z is the distance normal to the wall.

Normalizing this profile by the velocity at the top of the special element of thickness δ and scaling to the local dimensions of the element provides the shape function Φ^{s} from

$$[\Phi_1^{\mathrm{s}},\Phi_2^{\mathrm{s}}]=[1-A(\eta),A(\eta)], \tag{22}$$

with

$$A(\eta)=\frac{\ln[\delta(\eta+1)/2z_{\mathrm{o}}+1]}{\ln(\delta/z_{\mathrm{o}}+1)},\quad -1\leqslant\eta\leqslant 1,$$

where $\eta=-1$ at the wall and $\eta=1$ at the distance δ in the direction normal to the wall.
The two- and three-dimensional shape functions are obtained by the tensor product of the logarithmic shape function in the n_{w}-direction and the linear shape function in the other direction. A similar shape function is obtained for the enthalpy, while the species concentration is represented by the mother (trilinear/bilinear) shape function.

The eddy viscosity is obtained within the special element by differentiating equation (21), so that for constant shear stress across the element of $\rho(u^{+})^2$ we have

$$\nu_{\mathrm{eff}}=u_{*}\kappa(z+z_{\mathrm{o}}), \tag{23}$$

and u^{*} can be calculated by assuming local equilibrium in the near-wall region to give

$$u_{*}=c_{\mu}^{1/4}k^{1/2}, \tag{24}$$

where the value of k is available at the top of the special element from the solution in the main domain. The domain boundary for computations of k and ϵ is at the interface with the outer edge of the special element and the following boundary conditions are used:

$$\frac{\partial k}{\partial n}=0,\qquad \epsilon=\frac{(c_{\mu}^{1/2}k)^{3/2}}{\kappa\delta}. \tag{25}$$

Within the FEMSET formulation the special shape function is used to represent variables in the special element, while the mother shape function, rather than the special shape function as in Reference 18, is used for weighting. This makes it possible to conduct integrations with much lower-order quadrature than that used in FIDAP[19] for a similar treatment for smooth walls, while retaining the accuracy of the solution. The mother shape function is used in the temporal terms in the momentum and energy equations and in the continuity equation to retain symmetry of the pressure matrix. Although this causes degradation of continuity in the special element, it is thought to be better than imposing the condition of zero normal velocity as in the wall function approach. This treatment can be considered as an improved way of applying wall laws, yet without the need to leave a gap between the solution domain and the real boundary.

4. VALIDATION TESTS

The FEMSET model in its original form was validated against the two- dimensional wind tunnel tests of McQaid[20] and showed good agreement with the experiment. These validation tests were reported by Betts and El-Awad.[7] Simulation of the Burro-8 field trial over irregular ground topography using the model failed during the simulation of the wind field before the injection of the dense gas.[2] The Burro-8 test simulated over flat ground was successful in predicting the major features of the dense gas cloud qualitatively, but there were significant quantitative discrepancies with the experimental results.[4] The flat ground test was repeated in the present study with the modified near-ground treatment. This led to minor improvements in the cloud width and height owing to the better representation of the dense gas cloud in the near-ground region. These results were reported by Betts and Sayma.[21]

In the present study, simulation of the Burro-8 field trial over the original irregular topography was conducted and the simulation produced an acceptable agreement with the experimental results bearing in mind the uncertainties of the reported experimental results.

The Burro series of liquified natural gas (LNG) experiments was performed at the Naval Weapons Centre (NWC) at China Lake, California during the summer of 1980. The experiments included eight LNG dispersion tests with different spill volumes and spill rates under various atmospheric conditions. The experiments were initialized by spilling LNG onto the surface of a 1 m deep water pond. The spill pond is about 58 m in diameter; consequently, while the spill is onto water, most of the dispersion occurs over land. The ground topography of the test site around the pond is shown in Figure 1.

The Burro-8 test turned out to be the most interesting of the nine-test series. This test was conducted under moderate wind speed and slightly stable atmospheric conditions. This allowed the gently sloping terrain to affect the cloud behaviour significantly and the gravitational spreading effects to be pronounced. Since the moderate wind speeds leads to a low Froude number in this test

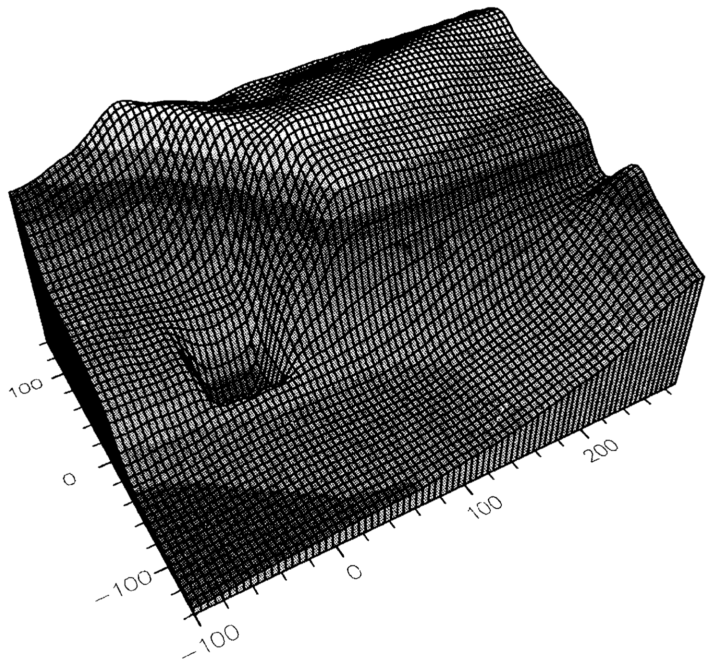

Figure 1. 3D perspective of ground topography of test site

case, the wind speed and turbulence levels were significantly affected by the cloud. Thus it was representative of typical spills of large scale where topography could affect the dense gas dispersion process. These were the main reasons which led to the selection of this test for validating the model.

A schematic diagram of the solution domain is shown in Figure 2. The x-axis was chosen to be aligned with the prevailing wind direction, the y-axis is the horizontal cross-wind direction and the z-axis is the vertical direction. Except for the plane adjacent to the ground, all the other boundary planes were chosen to be parallel to the principal co- ordinate planes to make the application of boundary conditions easier.

As initial conditions the following one-dimensional expressions were used for the vertical variation in the flow variables in the atmospheric layer:

$$u = \frac{u_*}{\kappa}\left[\ln\left(\frac{z - z_\mathrm{d} + z_\mathrm{o}}{z_\mathrm{o}}\right) + \psi(\zeta)\right], \tag{26a}$$

$$v = 0, \tag{26b}$$

$$w = 0, \tag{26c}$$

$$c = 0, \tag{26e}$$

$$k = c_\mu^{-1/2} u_*^2 \phi_k(\zeta), \tag{26f}$$

$$\epsilon = \frac{u_*^3}{\kappa(z - z_\mathrm{d} + z_\mathrm{o})}\phi_\epsilon(\zeta), \tag{26g}$$

$$\rho = \frac{c_\mathrm{pa} M_\mathrm{a}[P_\mathrm{o} - \rho_\mathrm{o} g(z - z_\mathrm{d} + z_\mathrm{o})]}{Rh}. \tag{26h}$$

Empirical expressions were used for the functions $\psi(\zeta)$ and $\psi_h(\zeta)$, while expressions for $\phi_k(\zeta)$ and $\phi_\epsilon(\zeta)$ were obtained by assuming local equilibrium of turbulence as follows:

$$\psi(\zeta) = \phi(\zeta) - 1, \tag{27a}$$

$$\psi_h(\zeta) = \phi_h(\zeta) - 1, \tag{27b}$$

$$\phi_k(\zeta) = [\phi_\epsilon(\zeta)/\phi(\zeta)]^{1/2}, \tag{27c}$$

$$\phi_\epsilon(\zeta) = \phi(\zeta) - \zeta, \tag{27d}$$

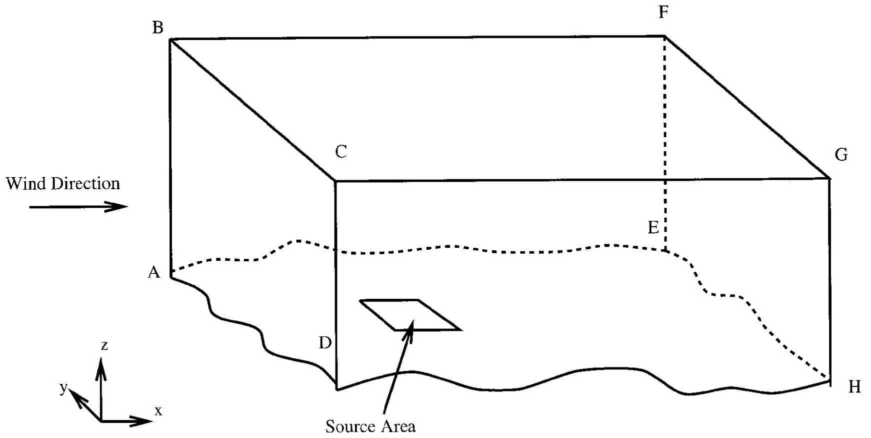

Figure 2. Schematic diagram of solution domain

where

$$\left.\begin{aligned}\phi(\zeta) &= (1{\cdot}0 - 20{\cdot}6\zeta)^{1/4}\\ \phi_h(\zeta) &= 1{\cdot}015(1{\cdot}0 - 12{\cdot}35\zeta)^{-1/2}\end{aligned}\right\}\quad \zeta < 0, \tag{28a}$$

$$\left.\begin{aligned}\phi(\zeta) &= 1 + 6{\cdot}45\zeta\\ \phi_h(\zeta) &= 1{\cdot}015 + 8{\cdot}85\zeta\end{aligned}\right\}\quad \zeta \geqslant 0. \tag{28b}$$

Equations (27) and (28) were obtained from Reference 14, but modified in this study following the remarks of Gibson and Launder.[13]

In the above system of initial conditions the following data of the Burro-8 field test were used: $u_* = 0{\cdot}074$ m s^{-1}, $q_a = -2{\cdot}2$ W m^{-2}, $h_* = 60{\cdot}3$ J kg^{-1}, $h_o = 3{\cdot}075$ J kg^{-1}, $z_o = 2{\cdot}05 \times 10^{-4}$ m. This system of initial conditions was also used as the boundary conditions at the inlet plane ABCD (see Figure 2).

Over the top plane BCGF the following boundary conditions were applied:

$$\rho K_{xz}\left(\frac{\partial u}{\partial z} + \frac{\partial w}{\partial x}\right) = \rho u_*^2, \tag{29a}$$

$$\left(\frac{\partial v}{\partial z} + \frac{\partial w}{\partial y}\right) = 0, \tag{29b}$$

$$-p + 2\rho K_{zz}\frac{\partial w}{\partial z} = 0, \tag{29c}$$

$$\rho K_z^h \frac{\partial h}{\partial z} = -q_a, \tag{29d}$$

$$\frac{\partial c}{\partial z} = 0, \tag{29e}$$

$$k = c_\mu^{-1/2} u_*^2 \phi_k(\zeta), \tag{29f}$$

$$\epsilon = u_*^3 \phi_\epsilon(\zeta)/\kappa(z - z_d). \tag{29g}$$

On the side planes ABFE and CDHG the following boundary conditions were applied:

$$\left(\frac{\partial u}{\partial y} + \frac{\partial v}{\partial x}\right) = 0, \tag{30a}$$

$$v = 0, \tag{30b}$$

$$\left(\frac{\partial w}{\partial y} + \frac{\partial v}{\partial z}\right) = 0, \tag{30c}$$

$$\frac{\partial h}{\partial y} = \frac{\partial c}{\partial y} = \frac{\partial k}{\partial y}\frac{\partial \epsilon}{\partial y} = 0. \tag{30d}$$

On the plane EFGH the following boundary conditions were applied:

$$-p + 2\rho K_{xx}\frac{\partial u}{\partial x} = -\tilde{p}, \tag{31a}$$

$$\left(\frac{\partial v}{\partial x} + \frac{\partial u}{\partial y}\right) = 0, \tag{31b}$$

$$w = 0, \tag{31c}$$

$$\frac{\partial h}{\partial x} = \frac{\partial c}{\partial x} = \frac{\partial k}{\partial x} = \frac{\partial \epsilon}{\partial x} = 0, \tag{31d}$$

where the value of the pressure $\tilde{p}$ is approximated by extrapolating the pressures from the last two cross-stream slices of elements at the previous time step.

Over the ground boundary the following boundary conditions were used:

$$u = 0, \qquad v = 0, \tag{32a}$$

$$w = 0 \quad \text{(except over the spill area during injection)}, \tag{32b}$$

$$h = h_o, \tag{32c}$$

$$n_i \frac{\partial c}{\partial x_i} = 0. \tag{32d}$$

Finally, over the spill source the boundary conditions over the bottom plane described earlier were used prior to and after the termination of injection and for all the variables except w, h and c during injection. For these variables the following boundary conditions were used during injection:

$$w = \begin{cases} 0 & \text{for } t \leqslant -10, \\ (10 + t)w_I/10 & \text{for } -10 \leqslant t < 0, \\ w_I & \text{for } 0 \leqslant t < 110, \\ (120 - t)w_I/10 & \text{for } 110 \leqslant t < 120, \\ 0 & \text{for } t \geq 120, \end{cases} \tag{33a}$$

$$h = c_{pg} \times T_g = 2100 \times 113 \text{ J kg}^{-1}, \tag{33b}$$

$$c = 1{\cdot}0, \tag{33c}$$

where $w_I = 0{\cdot}064$ m s^{-1} is the steady state value of the vertical injection velocity of the gas and T_g and c_{pg} are the boil-off temperature and gas specific heat at constant pressure of LNG respectively. The time origin ($t = 0$) is the instant the injection velocity reaches its steady state. This nominally is equivalent to the time when the valve is fully opened in the experiment.

4.1. *Results of the dense gas simulation*

In this simulation the solution domain extended from 100 m upstream of the centre of the spill pond to 290 m downstream. In the cross-stream direction the solution domain extended from 140 to 140 m (the origin of the co-ordinate system was in the centre of the spill pond). The solution domain extended vertically to 18 m above the datum level, which was the water surface at the spill pond. A three- dimensional perspective of the solution domain is shown in Figure 1, while two sections in the mesh are shown in Figures 3 and 4. The number of elements used was $32 \times 30 \times 12$ in directions x, y and z respectively. A total of 48 elements spanned the spill pond, with six elements in the x-direction and eight elements in the y-direction. The first element spacing from the ground ranged from 0·07 to 0·14 m. The mesh used contained 11,520 elements and 13,299 nodal points.

Since the initial conditions do not satisfy continuity, a disturbance occurred at the first time step of the wind field simulation which caused some wiggles in the velocity field. These wiggles smoothed and washed through the solution domain. The simulation of the domain wind field before injecting the dense gas required 2000 time steps. Figure 5 shows a vector plot of the velocity field on the plane $y = 0$. Although there is still a trace of the wiggles downstream, it was decided to start injection at this stage, since these wiggles will be washed away long before the arrival of the dense gas cloud.

No problems were encountered throughout the injection period of the dense gas and the results were recorded every 20 s of the transient solution to enable comparisons with the experimental results. After termination of the injection, severe spatial wiggles were created locally at and around the spill pond. The exact reason for these wiggles is not known, but it was thought to be a result of a

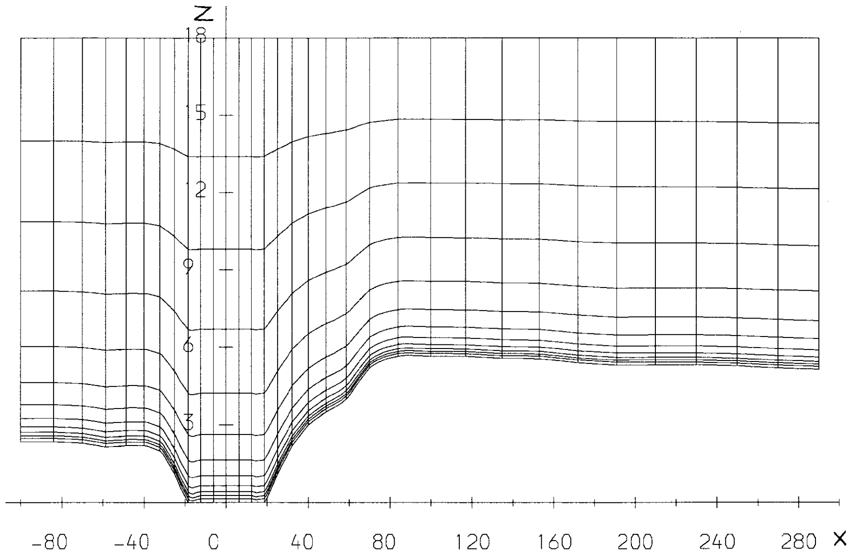

Figure 3. Cross-section in mesh parallel to *x*–*z* plane at $y = -12$ m (note magnification in *z*-direction)

combination of the relatively coarse mesh around the pond and the over-rapid reduction of the vertical injection velocity during the shutdown of the source. The vertical injection velocity at the pond convected a certain level of turbulence which decreased rapidly during shutdown of the source, and the cross-wind coarse mesh was not able to cope with these rapid temporal variations. This is evident from the gradual decay of the wiggles when the simulation was continued beyond this time level and the shear stress over the pool increased. The simulation was continued and the wiggles died

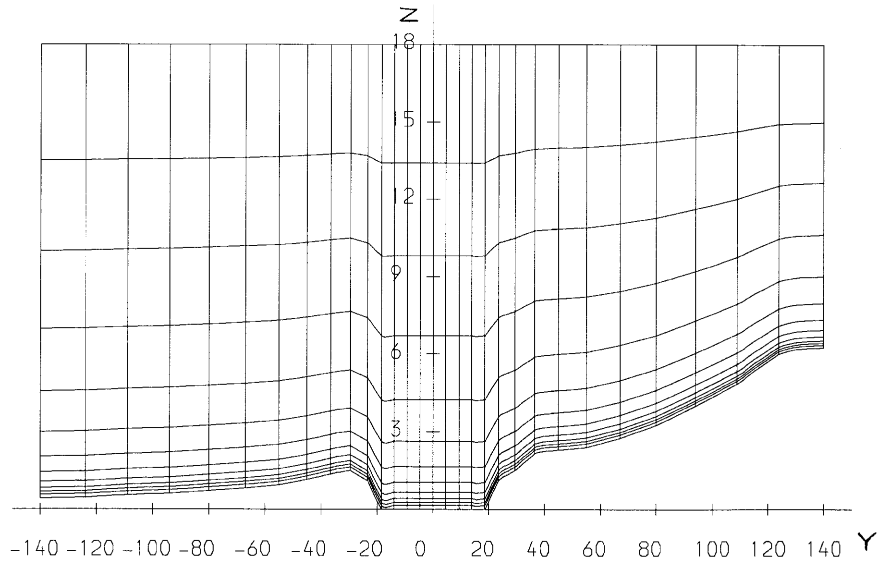

Figure 4. Cross-section in mesh parallel to *y*–*z* plane at $x = 18$ m (note magnification in *z*-direction)

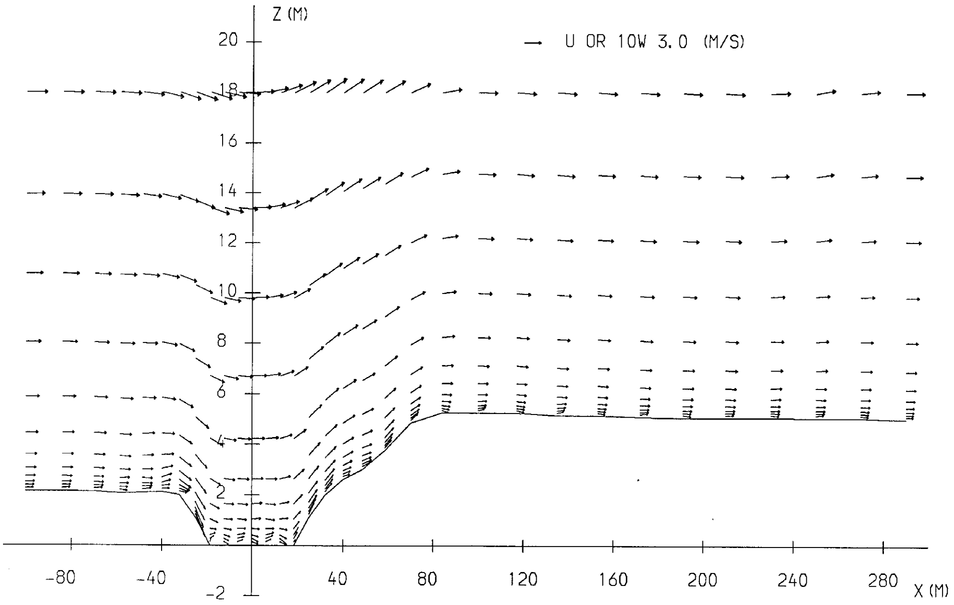

Figure 5. Velocity field at $y=0$ before starting injection of dense gas (note magnification in z-direction)

out completely at time level 200 s. Finally, the simulation process was terminated at time level 300 s. Ideally, the simulation should have been continued until the dense gas cloud washed out completely from the domain, but computer resource limitations did not allow that.

Before presenting the results, it should be noted that the calculated concentrations c in the present model are mass fractions of the dense gas, while the measured concentrations in the Burro tests were volume fractions. Thus the present results were converted to volume fractions, which are also referred to here as volume concentrations, to enable comparisons with the experimental results.

Figure 6 shows the volume concentration contours at 1 m height above ground level for time levels 20, 80, 120, 140, 200 and 260 s. Figure 7 shows the volume concentration contours over the vertical plane $y=0$ for the same time levels, while Figure 8 shows the concentration contours on vertical planes normal to the x-axis at different x-positions for the same time levels.

The simulation showed the ability of the model to reproduce the major features of a large-scale dense gas spill both qualitatively and quantitatively. A qualitative assessment will be considered first; the quantitative comparisons will follow.

From the early stages of the spill, lateral spreading and upwind movement of the cloud were noticed. This was obvious in the velocity field and concentration contour plots. Movement towards the low ground at the left-hand side of the pond looking upstream can also be seen at this stage from the concentration contour of Figure 6(a). The beginning of plume bifurcation can also be noticed at this stage. The relatively high ratio of cross-wind velocity to ambient velocity caused bifurcation of the cloud, which was also noticed in the aerial photographs taken during the experiment. The vector plots also showed decoupling of the cloud from the wind shear even at this early stage. This can be seen from the vertical injection of the gas, which would have been at a smaller angle with the horizontal if it were affected directly by the ambient wind. This causes the gas to rise above ground level to a certain height and pour to the ground in all directions, causing the noticed upwind movement of the cloud. The obstruction to the ambient wind resulting from the cloud caused an upward movement oof the flow upwind of the spill pond, resulting in the elevated head of the cloud at

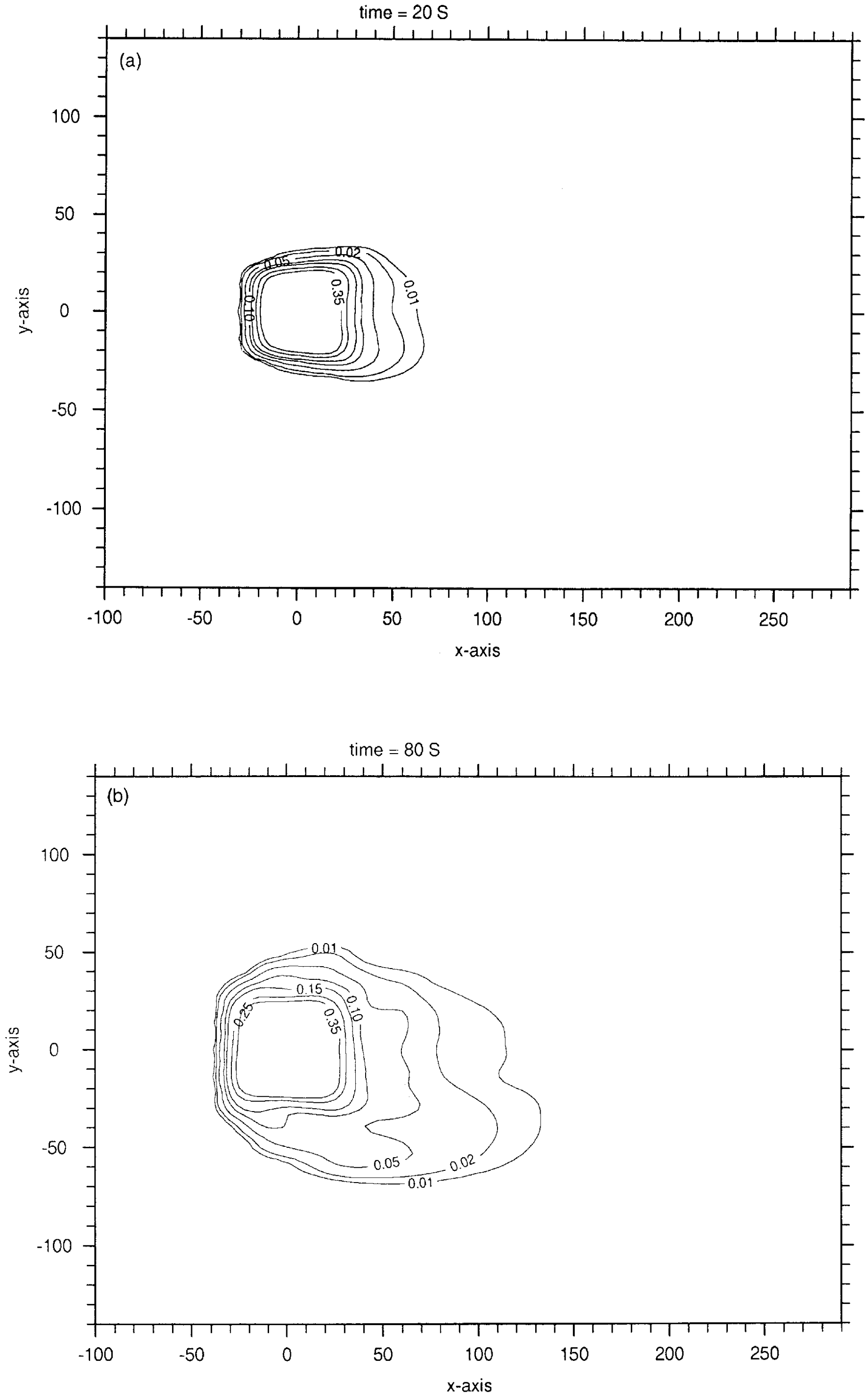

Figure 6. Horizontal volume concentration contours at 1 m height above ground level at different time levels

the front which can be seen from the vertical concentration contours of Figure 7. Close packing of the

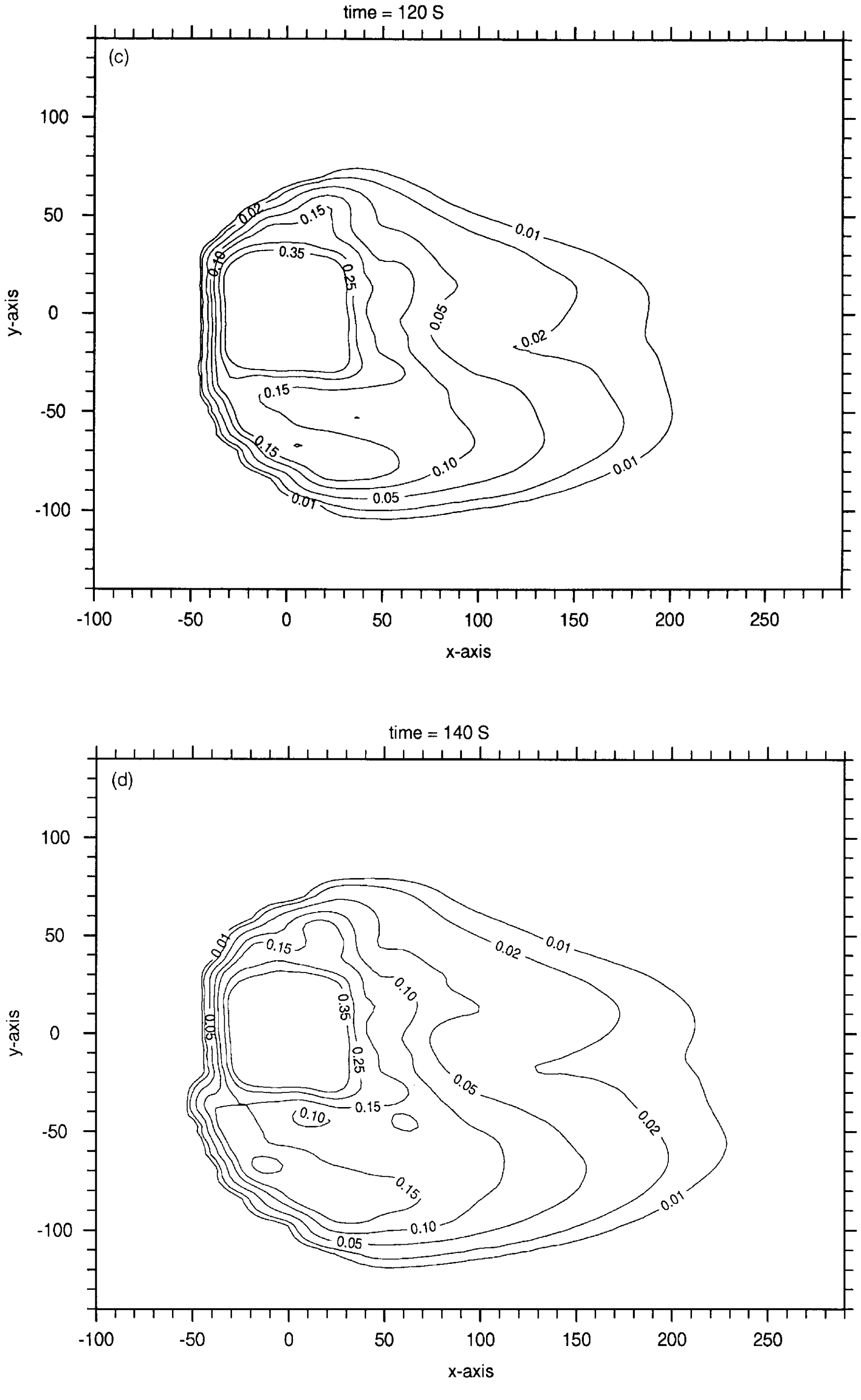

Figure 6. (*continued*)

contours upwind of the cloud is also noticeable, which is a result of the upwind movement of the cloud being opposed by the ambient wind.

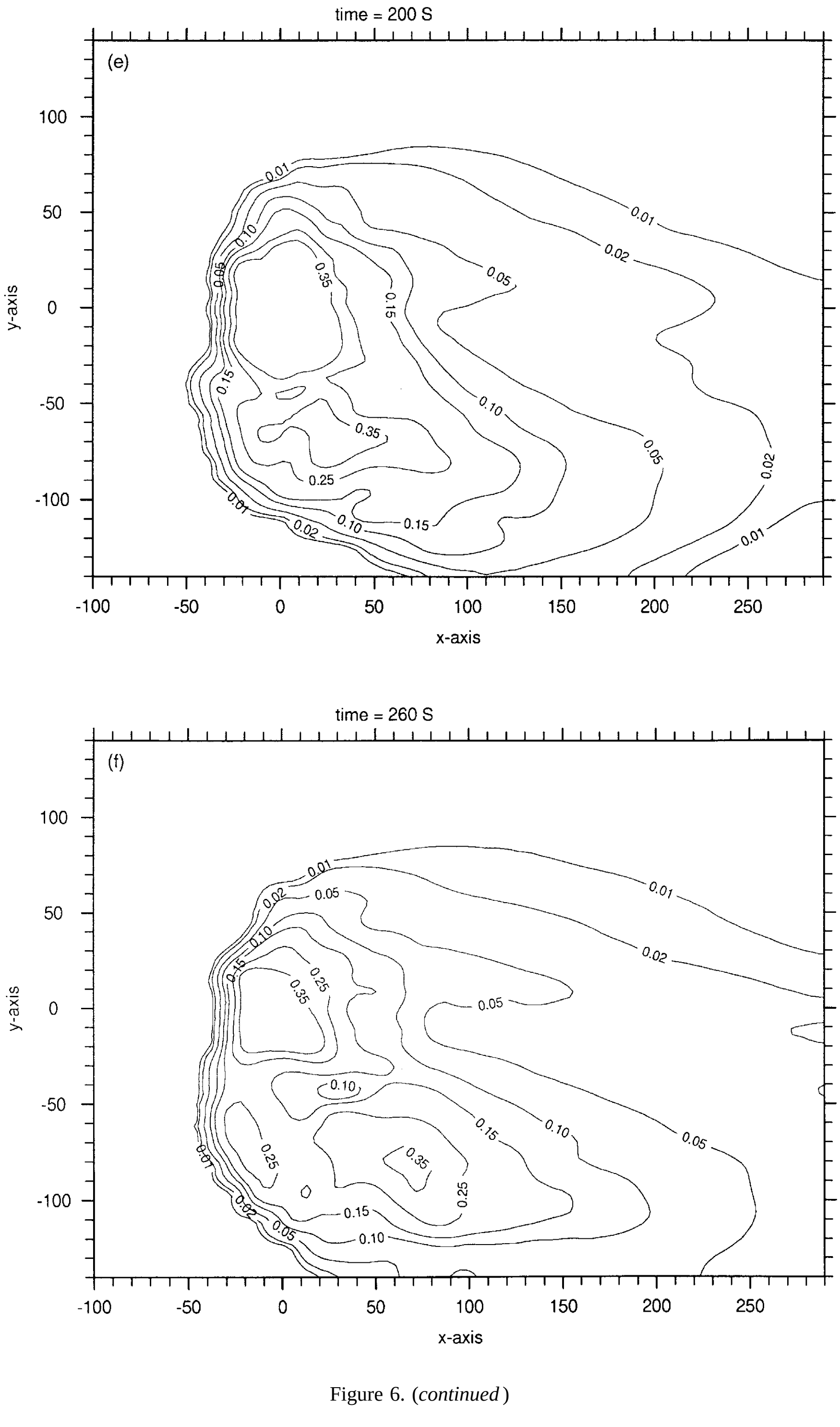

Figure 6. (*continued*)

At the later stages of the spill the above effects were seen to increase. The cloud bifurcation and the

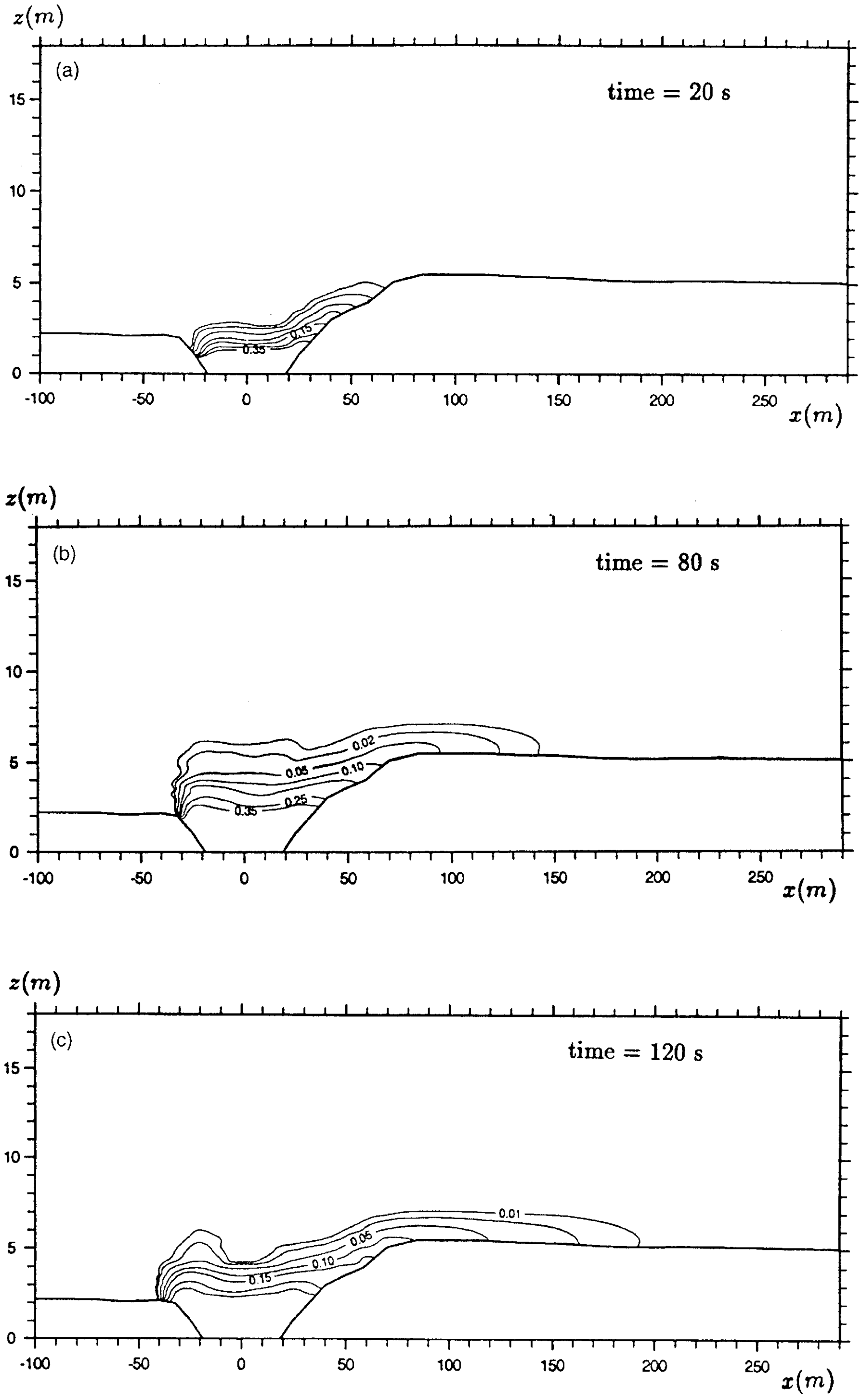

Figure 7. Vertical volume concentration contours at plane $y = 0$ at different time levels

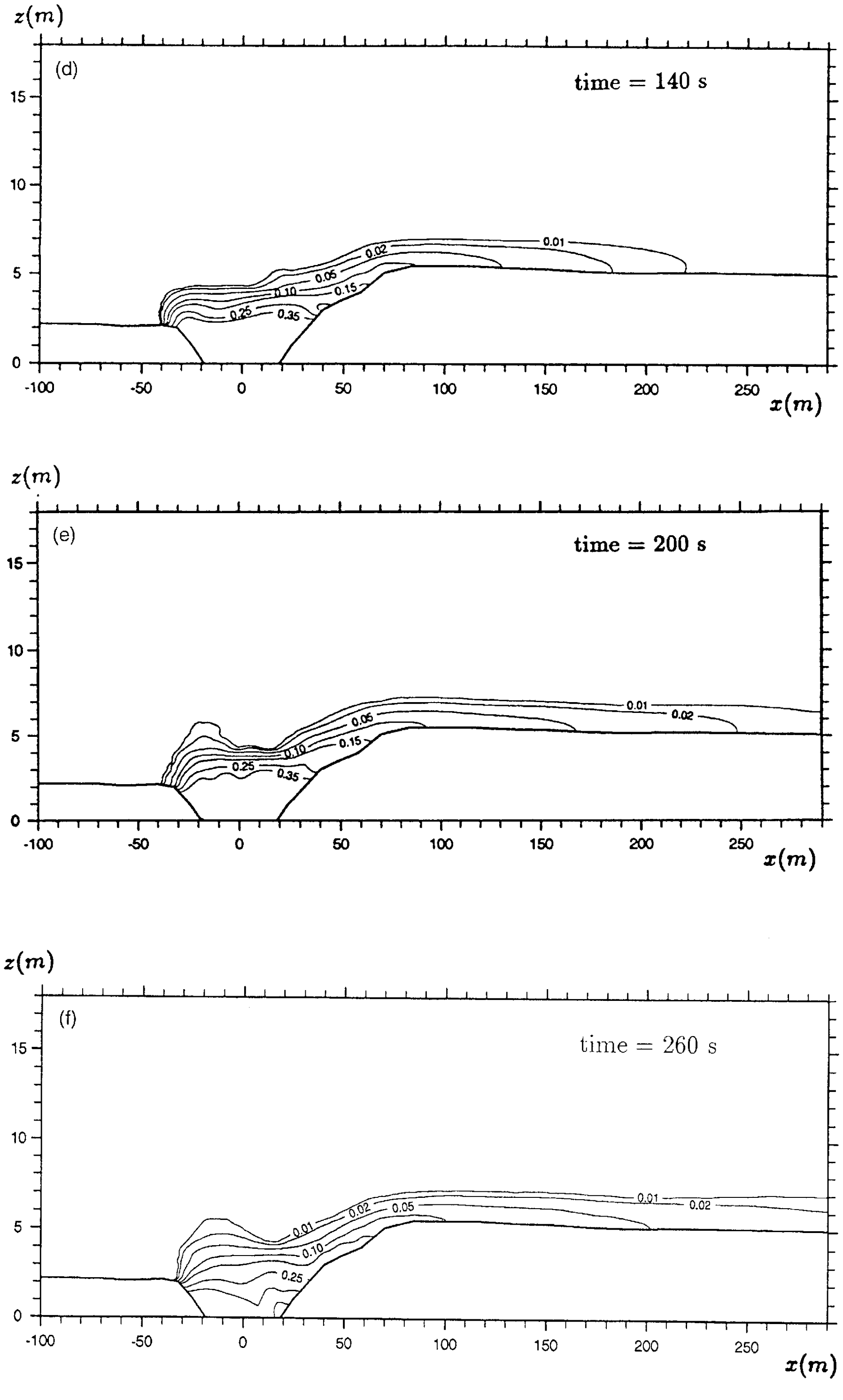

Figure 7. (*continued*)

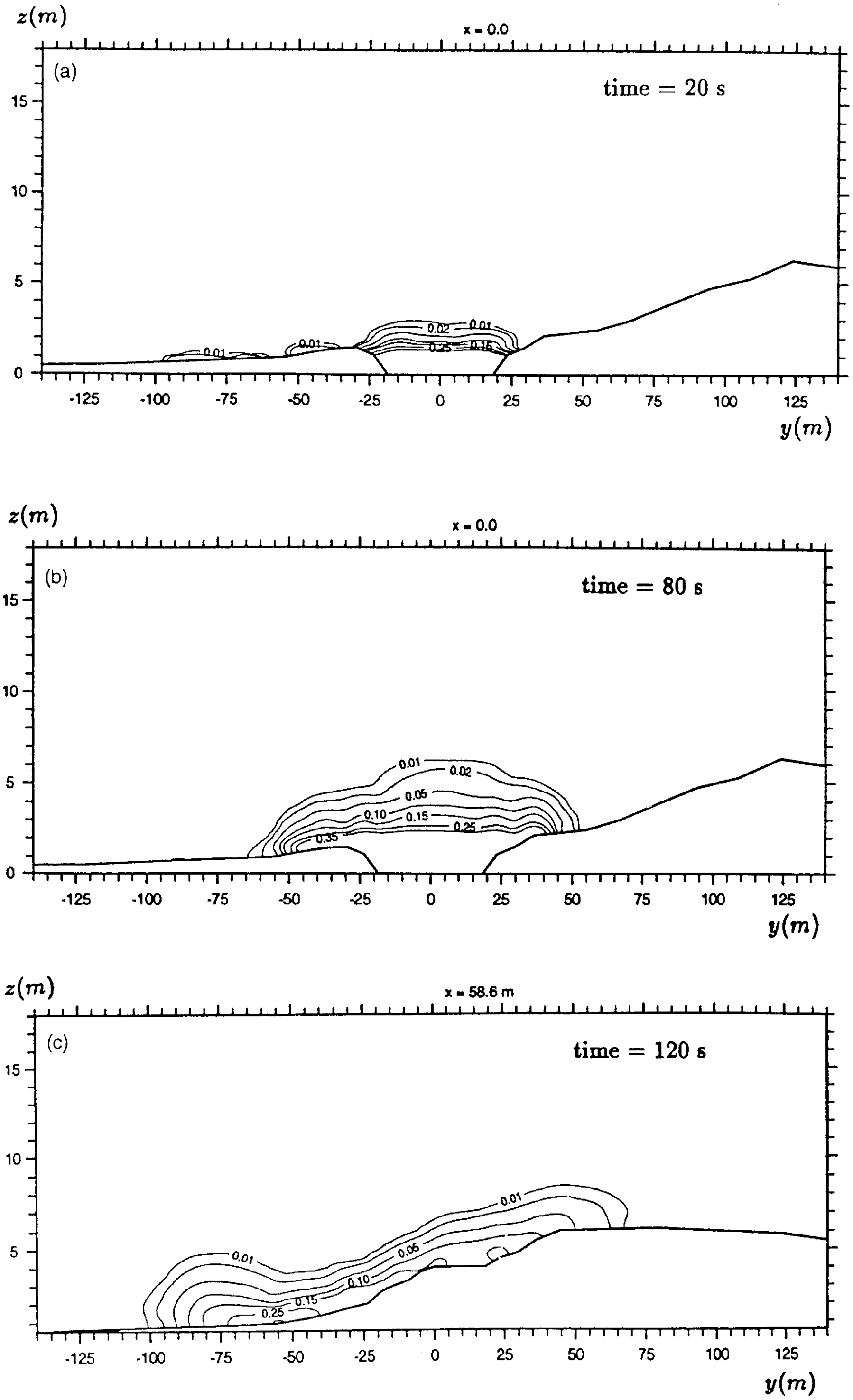

Figure 8. Vertical volume concentration contours at planes parallel to $x = 0$ at different time levels

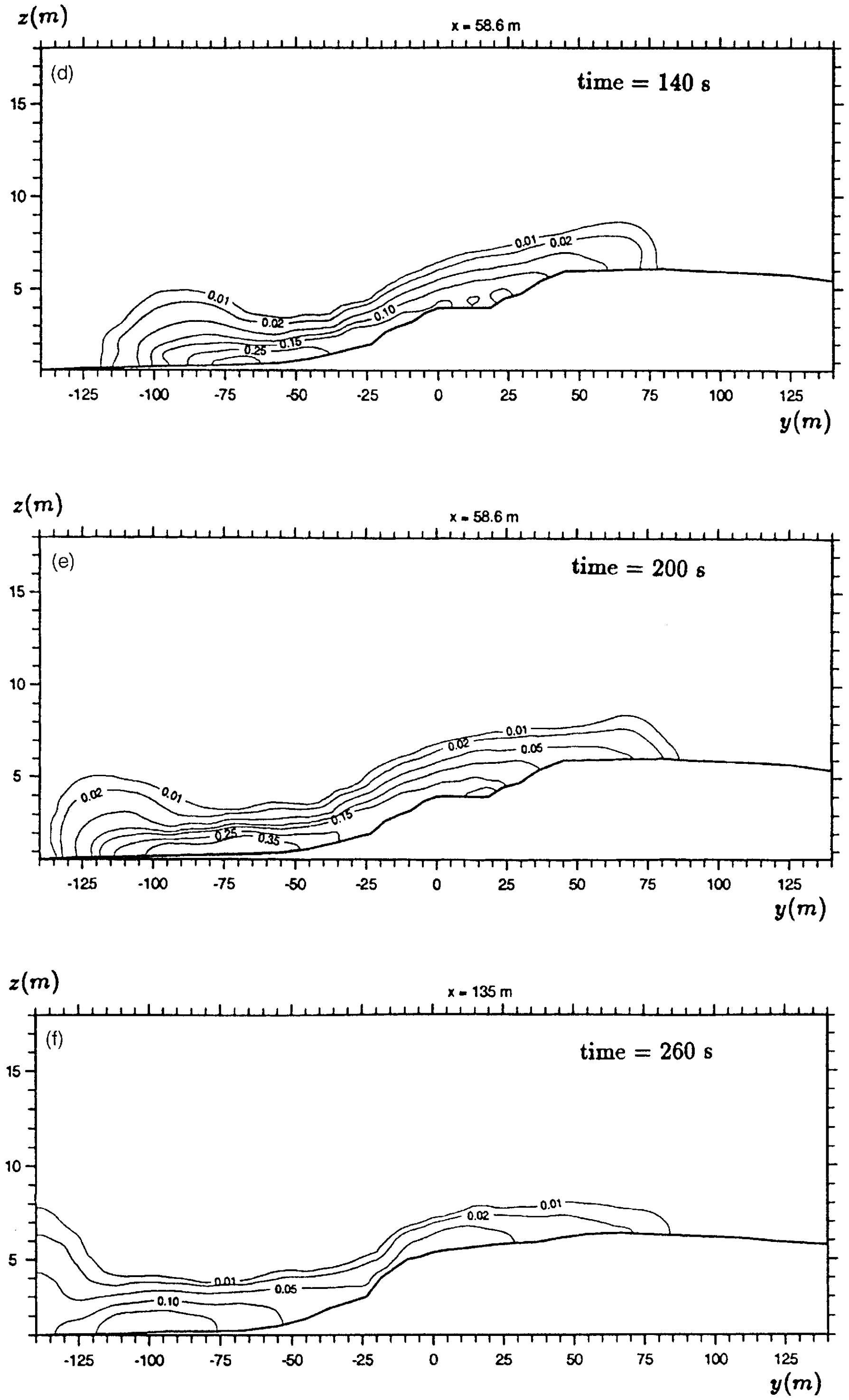

Figure 8. (*continued*)

rolling towards the low ground became more noticeable, while the height of the cloud only increased slightly. The upwind movement of the cloud was seen to increase gradually up to a stationary distance of 40 m from the edge of the pond.

The cloud lingered above the spill source at least up to the time level 300 s when the simulation was terminated, although concentration contours show that the cloud started to leave the domain and move downwind of the source. It seems that the simulated cloud stayed slightly longer than reported in the experiment over the source. The wiggles resulting after the termination of the injection and the strong collapse of turbulence over the pond are thought to be behind the delay of the cloud movement.

Quantitatively, there was reasonable agreement with the experimental results to within the limitations and accuracy of the reported experimental results. The concentration contours of the Burro-8 results were plotted using logarithmic interpolation of the concentrations from the sparsely distributed sensors. For one time level, 160 s (where linear interpolation contours were reported), the report showed considerable differences if the contours were plotted using linear interpolation. However, because the logarithmic interpolation produced more conservative results, it was used throughout the report. The results of the present simulation showed predicted results halfway between the results of logarithmic interpolation and linear interpolation for that time level.

Figure 9 shows the maximum distance travelled by the lower flammability level (LFL) contour (5% volume concentration) compared with the experimental results. This figure also shows the point where the linear interpolation was used and the results of the flat ground simulation performed using FEMSET.[21] Although the results of the irregular topography simulation have considerable differences at intermediate points between sensors, the results have good agreement with the experiment at positions near experimental sensors (57 m arc and 140 m arc shown in the figure). This gives rise to the point that the logarithmic interpolation produced excessively conservative results and that the present simulation produced good agreement with the experiment. This can also be seen from the time history of the concentrations at two different sensors shown in Figures 10 and 11, where good agreement between the experimental results and the present simulation is obvious. It should be noted here that over most of the cloud the typical height of the cloud was about 1 m, which is the height at which the field test transducers were placed. The top of the cloud is a region of strong vertical gradient of concentration. Hence small errors in the computation of the cloud height have the potential for massive changes in the arrival time of the LFL. Under these circumstances the agreement with the field data is remarkably good.

The Burro-8 data for ground heat flux are available at only two positions, G04 and 57 m and G06 at 140 m from the pond centre. The sensor G04 indicated a maximum heat flux of 400 W m^{-2} at 110 s, but also indicated a value of 140 W m^{-2} before the arrival of the cloud instead of a small negative value of 2·2 W m^{-2} (the reported level of ambient heat flux of the Burro-8 test). The sensor G06 produced a maximum heat flux of 180 W m^{-2} at time level 180 s, while the heat flux was 100 W m^{-2} before the arrival of the cloud. In the present simulation, where the positions of storing the data are slightly different from the sensor positions, the results at the position closest to sensor G04 showed heat fluxes of 7·1, 3·8 and 1·6 W m^{-2} at time levels 100, 180 and 300 s respectively. At the position nearest to sensor G06 the heat fluxes were 0·18, 1·42 and 0·22 W m^{-2} at the same time levels. In interpreting these results, two factors should be remembered. Firstly, the sensor values are abnormally high before the cloud arrival mentioned above. Secondly, at some time levels and positions the equation $q_{\mathrm{n}} = \kappa \rho c_{\mu}^{1/4} k^{1/2} (h_{\mathrm{o}} - h) \ln(\delta / z_{\mathrm{o}})$ used to calculate the heat flux is not applicable owing to the collapse of turbulence and thus it produced low values of the simulated results. Extensive investigation of the heat transfer aspects would require the correct level of turbulence and more reliable experimental results.

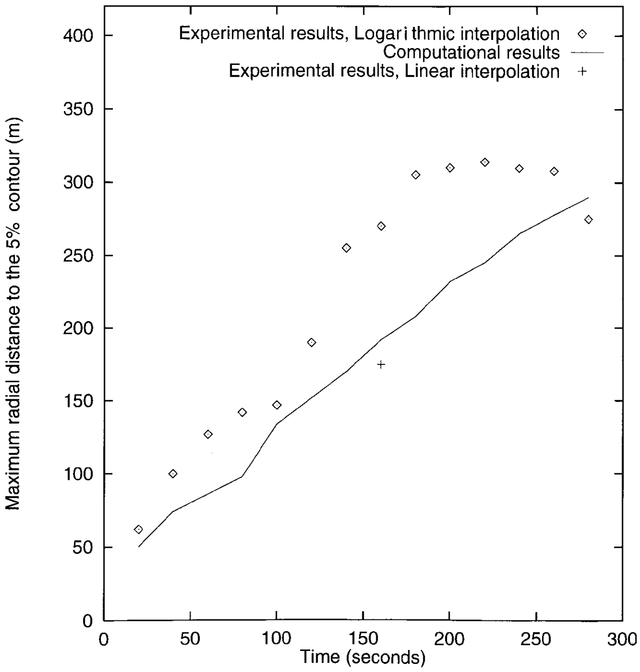

Figure 9. Maximum radial distance travelled by lower flammability limit contour

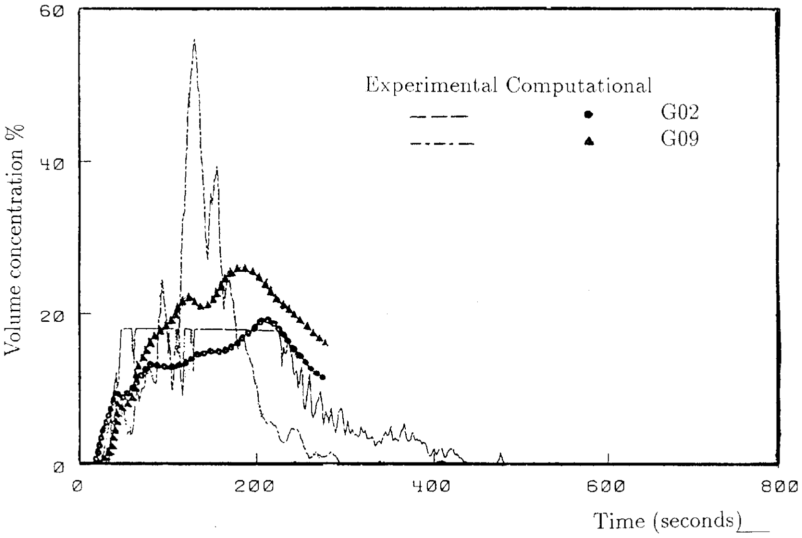

Figure 10. Time history of concentration at two sensor stations at arc 57 m

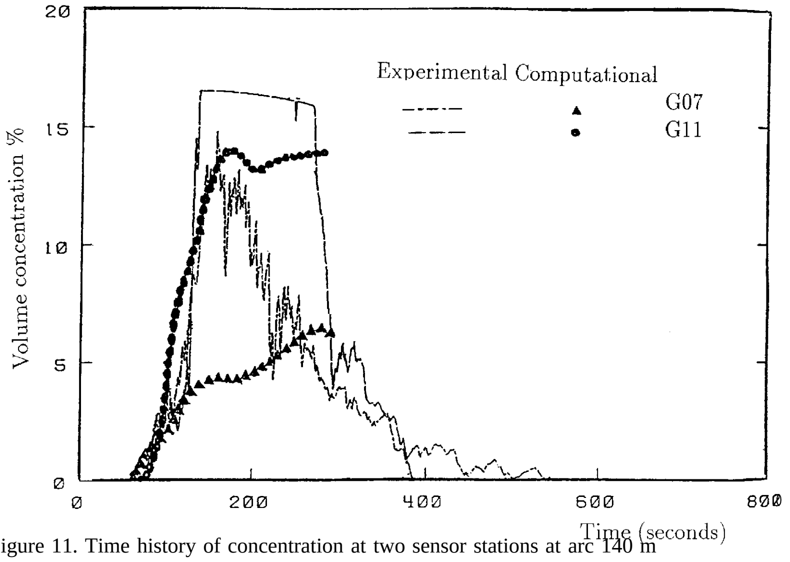

Figure 11. Time history of concentration at two sensor stations at arc 140 m

5. CONCLUSIONS

The numerical simulation reported has shown the capability of the computer model in predicting large-scale dense gas dispersion accidents with reasonable accuracy. It was also demonstrated that the two-equation turbulence model with extensions allowing for the prediction of the effects of stratification produced good results without imposing case-specific empirical turbulence correctors as would be required if a less sophisticated turbulence model were used. Moreover, the results demonstrated that the numerical algorithm can apply this model on a mesh that does not have to be excessively refined in the vertical direction to retain stability. The differences between the results obtained and the reported experimental results are considered to be within the uncertainty range of the reported experimental results. However, the simulation identified several points for further investigation and development in the model. The local collapse of turbulence in some regions leads to the suggestion of using a low-Reynolds-number turbulence model. The non-linear eddy viscosity model would be a potential candidate, since second-moment closure models might require impractical computational times. Furthermore, improved modelling is required for the effects of ground heat transfer, which might include submodels for heat conduction in the ground. The desert tests of Burro-8 were under conditions of low atmospheric humidity. To enable the model to predict a wider range of scenarios, where the effects of water vapour condensation may be significant, a suitable submodel with an additional transport equation could be implemented. Further developments are desirable in the numerical solution procedure to reduce the high computational costs, e.g. the use of the conjugate gradient method for the pressure solution and the possible use of adaptive meshing to better resolve the moving high-gradient regions such as the front of the cloud.

APPENDIX: NOMENCLATURE

b	buoyancy generation/destruction term
c	mass fraction

$\mathbf{c}$	global vector containing nodal values of c
c_μ, $c_{\epsilon 1}$, $c_{\epsilon 2}$, $c_{\epsilon 3}$	emperical coefficients in k– ϵ model
c_p, c_pa, c_pg	specific heats at constant pressure of gas mixture, ambient air and contaminant gas
$\mathbf{C}$	pressure gradient matrix operator
$\mathbf{C}^\mathrm{T}\mathbf{M}^{-1}\mathbf{C}$	consistent Poisson pressure matrix
$\mathbf{D}$	velocity divergence matrix operator
$\mathbf{f}$	load vector in discretized momentum equation
$\mathbf{f}_\theta$	load vector in discretized θ-equation ($\theta = h, c, \rho, k, \epsilon$)
g	gravitational acceleration constant
h	specific static enthalpy
h_o	ground surface enthalpy
h_*	ambient friction enthalpy, $q_\mathrm{a}/\kappa u_* \rho c_\mathrm{pa}$
h^+	h/h_*
k	turbulent kinetic energy
K_{ijlm}	fourth-order eddy viscosity tensor
K_{ij}^θ	second-order eddy diffusivity tensor ($\theta = h, c, \rho, k, \epsilon$)
L	Monin–Obukhov length scale, $-u_*^3 \rho h_\mathrm{o}/\kappa g q_\mathrm{a}$
$\mathbf{M}$	mass matrix in discretized momentum equation
M_a, M_g	molecular weights of ambient air and contaminant gas
$\mathbf{M}_\theta$	mass matrix in discretized θ-equation ($\theta = h, c, k, \epsilon$)
$\mathbf{M}_\rho$	mass matrix in continuity equation
n_w	direction normal to wall
p	deviation pressure
$\mathbf{p}$	global vector containing nodal values of p
$\tilde{p}$	pressure approximated by projection to wall
P	thermodynamic pressure
P_o	reference absolute pressure
Pr_θ	turbulent Prandtl number ($\theta = h, \rho, k, \epsilon$)
q_a	ambient heat flux from underlying ground
R	universal gas constant
s	shear generation term in k-equation
Sc	turbulent Schmidt number
S_h	source term in energy equation
t	time
T	absolute temperature
u, v, w	three components of velocity vector in Cartesian co-ordinate frame
U, V, W	three components of vector ρu_i ($i = 1, 2, 3$)
$\mathbf{U}$	global vector containing nodal values of U, V and W
u_*	ambient friction velocity
u^+	u/u_*
$\overline{u_i' c'}$	turbulent mass flux vector
$\overline{u_i' h'}$	turbulent enthalpy flux vector
$\overline{u_i' u_j'}$	Reynolds stress tensor
w_I	maximum gas injection velocity
x, y, z	three axes of global Cartesian co-ordinate frame
z_d	height of ground above fixed datum level
z_o	ground surface roughness scale

Greek letters

δ	normal distance between boundary of computational domain and nearby solid surface
δ_{ij}	Kronecker delta
t	time step
ϵ	viscous dissipation rate of k
ζ	$z - z_{\mathrm{d}}/L$
η	local dimension of special shape function in n_{w}- direction
κ	von Karman constant
ν, ν_{t}	kinematic molecular viscosity, kinematic eddy viscosity
ν_{eff}	effective viscosity, $\nu + \nu_{\mathrm{t}}$
ρ	density
$\boldsymbol{\rho}$	global vector containing nodal values of ρ
ρ_{o}	reference density at which gravity force is zero
$\phi(\zeta)$, $\phi_h(\zeta)$	dimensionless gradients of wind speed and enthalpy in atmospheric surface layer
$\phi_k(\zeta)$, $\phi_c(\zeta)$	dimensionless profiles of k and ϵ in surface layer
Φ^{s}	special element shape function
$\psi(\zeta)$, $\psi_h(\zeta)$	functions of $\phi(\zeta)$ and $\phi_h(\zeta)$

Superscripts

$(\ )^n$	time level of time-stepping solution algorithm
$(\ )^{-1}$	matrix inversion
$(\ )^{\mathrm{T}}$	transpose of matrix
$(\dot{\ })$	partial differentiation with respect to time

Abbreviations

BTD	balancing tensor diffusivity
FEM	forward Euler method
LFL	lower flammability level
LNG	liquified natural gas

REFERENCES

1. R. E. Britter and J. M. McQuaid, 'Workbook on the dispersion of dense gases', *Tech. Rep. 17/1988*, Health and Safety Executive (HSE), London, 1988.
2. V. Haroutunian, 'A time-dependent finite element model for atmospheric dispersion of gases heavier than air', *Ph.D. Thesis*, University of Manchester, 1987.
3. C. J. Wheatley and D. M. Webber, 'Aspects of the dispersion of heavier-than-air vapour relevant to gas explosions', *Tech. Rep. XII/829/84-EN, Contract Rep. SR/007/80/UK/HEAEC/UKAEA*, 1984.
4. P. L. Betts and V. Haroutunian, 'Finite element calculations of transient dense gas dispersion', in J. S. Puttock (ed.), *Stably Stratified Flow and Dense Gas Dispersion*, Clarendon, Oxford, 1988, pp. 349- -384.
5. P. L. Betts and V. Haroutunian, 'A *k*–ϵ finite element simulation of buoyancy effects in the atmospheric surface layer', *Proc. ASME Winter Meet. 83-WA/HT-32*, ASME, New York, 1983.
6. P. L. Betts and V. Haroutunian, '*k*–ϵ modelling of turbulent flow over a backward facing step by a finite element method', *Proc. 4th Int. Conf. on Numerical Methods in Laminar and Turbulent Flow*, Pineridge, Swansea, 1985, pp. 574–585.
7. P. L. Betts and M. M. El-Awad, 'Stability effects on dense gas dispersion: validation of turbulence model', in C. Taylor, J. H. Chin and G. M. Homsy (eds), *Proc. 7th Int. Conf. on Laminar and Turbulent Flows*, Stanford, CA, 1991, Pineridge, Swansea, 1991, pp. 212–221.
8. R. P. Koopman *et al*., 'Burro series data report LLNL/NWC 1980 LNG spill tests', *Tech. Rep. UCID-19075*, Lawrence Livermore National Laboratory, 1982.

9. S. F. Jagger, 'Formulation of the dense gas dispersion problem', in S. Hartwing (ed.), *Proc. 2nd Symp. on Heavy Gases and Risk Assessment*, Frankfurt am Main, 1982.
10. R. L. Peterson and M. A. Radcliff, 'Effects of homogeneous and heterogeneous surface roughness on HTAG dispersion', *Tech. Rep.*, API, Washington, DC, 1989.
11. Y. Riou, 'The use of a three-dimensional model for simulating Thorney Island field trails', in J. S. Puttock (ed.), *Stably Stratified Flow and Dense Gas Dispersion*, Oxford University Press, Oxford, 1988, pp. 323– 348.
12. S. T. Chan, 'FEM3A, a finite element model for the simulation of gas transport and dispersion', *LLNL-UCLRL-21043*, Lawrence Livermore National Laboratory, 1988.
13. M. M. Gibson and B. E. Launder, 'Ground effects on the pressure fluctuations in the atmospheric boundary layer', *J. Fluid Mech.*, **86**, 491–511 (1978).
14. J. A. Businger *et al*., 'Flux-profile relationships in the atmospheric surface layer', *J. Atmos. Sci.*, **28**, 181 (1971).
15. W. Rodi, 'Calculation of stably stratified shear-layer with a buoyancy-extended k–ϵ turbulence model', *Inst. Math. Appl. Conf. Ser.*, 111–140 (1985).
16. P. M. Gresho, S. T. Chan, R. L. Lee and C. D. Upson, 'A modified finite element method for solving the time-dependent incompressible Navier– Stokes equations. Part 1', *Int. j. numer. methods fluids*, **4**, 557 (1984).
17. P. M. Gresho, L. E. Lee and R. L. Sani, 'Advection dominated flows with emphasis on the consequences of mass lumping', in R. H. Gallagher *et al*. (eds), *Finite Elements in Fluids*, Vol. 3, Wiley, New York, 1978, pp. 27–79.
18. V. Haroutunian and M. S. Engelman, 'On modelling wall-bound turbulent flows using specialized near-wall finite elements and the standard k– ϵ turbulence model', *ASME, FED*, **117**, 27–79 (1991).
19. *FIDAP*, *Fluid Dynamics Analysis Package*, *V 5.0*, Fluid Dynamics International, Evanston, IL, 1991.
20. J. McQuaid, 'Some experiments on the structure of stably-stratified shear flow', *Tech. Paper P21*, Safety in Mines Research Establishment, 1976.
21. P. L. Betts and A. I. Sayma, 'Improved near ground treatment in finite element simulation of dense gas dispersion', in K. Morgan *et al*. (eds), *Finite Elements in Fluids*, Pineridge, Swansea, 1993, pp. 959–969.